HHS Public Access

Author manuscript

Science. Author manuscript; available in PMC 2021 June 11.

Published in final edited form as:

Science. 2019 March 29; 363(6434): . doi:10.1126/science.aau0135.

T cell stemness and dysfunction in tumors are triggered by a common mechanism

Suman Kumar Vodnala[#1,2], **Robert Eil**[#1,2,3], **Rigel J. Kishton**[1,2], **Madhusudhanan Sukumar**[1,2], **Tori N. Yamamoto**[1,2,4], **Ngoc-Han Ha**[5], **Ping-Hsien Lee**[1,2], **MinHwa Shin**[5,†], **Shashank J. Patel**[1,2,‡], **Zhiya Yu**[1,2], **Douglas C. Palmer**[1,2], **Michael J. Kruhlak**[6], **Xiaojing Liu**[7], **Jason W. Locasale**[7], **Jing Huang**[5], **Rahul Roychoudhuri**[8], **Toren Finkel**[9], **Christopher A. Klebanoff**[10,11,12], **Nicholas P. Restifo**[1,2,§]

[1]Surgery Branch, Center for Cancer Research, National Cancer Institute, Bethesda, MD 20892, USA.

[2]Center for Cell-Based Therapy, National Cancer Institute, Bethesda, MD 20892, USA.

[3]Department of Surgery, Memorial Sloan Kettering Cancer Center, New York, NY 10065, USA.

[4]Immunology Graduate Group, University of Pennsylvania, Philadelphia, PA 19104, USA.

[5]Laboratory of Cancer Biology and Genetics, National Cancer Institute, Bethesda, MD 20892, USA.

[6]Experimental Immunology Branch, National Cancer Institute, Bethesda, MD 20892, USA.

[7]Department of Pharmacology and Cancer Biology, Duke University School of Medicine, Duke University, Durham, NC 27710, USA.

[8]Babraham Institute, Babraham Research Campus, Cambridge, UK.

[9]Aging Institute, Department of Medicine, University of Pittsburgh School of Medicine, Pittsburgh, PA 15261, USA.

[10]Parker Institute for Cancer Immunotherapy, New York, NY 10065, USA.

[11]Center for Cell Engineering and Department of Medicine, Memorial Sloan Kettering Cancer Center, New York, NY 10065, USA.

[12]Weill Cornell Medical College, Cornell University, New York, NY 10065, USA.

[#] These authors contributed equally to this work.

[§]Corresponding author. restifon@mail.nih.gov.

[†]Present address: Department of Biochemistry and Molecular Biology, Korea University College of Medicine, Seoul, Korea.

[‡]Present address: Department of Cancer Immunology and Immune Modulation, Boehringer Ingelheim Pharmaceuticals Inc., Ridgefield, CT, USA.

Author contributions: S.K.V., R.E., and N.P.R. conceived the project and designed the experiments; S.K.V., R.E., and R.J.K. performed experiments and interpreted data; M.S., T.N.Y., N.-H.H., P.-H.L., M.H.S., S.J.P., Z.Y., D.C.P., M.J.K., J.H., X.L., J.W.L., and T.F. contributed in performing experiments and edited the manuscript; T.F. and C.A.K. provided intellectual but not experimental input in reporting the data; S.K.V., R.E., C.A.K., and N.P.R. wrote the manuscript; and N.P.R. supervised the project.

Competing interests: Authors declare no competing interests.

Data and materials availability: Datasets described in the paper are deposited in Gene Expression Omnibus (accession number GSE122156). S.K.V., R.E., R.J.K., and N.P.R. have submitted U.S. Provisional Patent Application 62/661,941, filed 24 April 2018, for the use of hydroxycitrate on T cells to improve efficacy of adoptive cell therapy.

Abstract

A paradox of tumor immunology is that tumor-infiltrating lymphocytes are dysfunctional in situ, yet are capable of stem cell–like behavior including self-renewal, expansion, and multipotency, resulting in the eradication of large metastatic tumors. We find that the overabundance of potassium in the tumor microenvironment underlies this dichotomy, triggering suppression of T cell effector function while preserving stemness. High levels of extracellular potassium constrain T cell effector programs by limiting nutrient uptake, thereby inducing autophagy and reduction of histone acetylation at effector and exhaustion loci, which in turn produces $CD8^+$ T cells with improved in vivo persistence, multipotency, and tumor clearance. This mechanistic knowledge advances our understanding of T cell dysfunction and may lead to novel approaches that enable the development of enhanced T cell strategies for cancer immunotherapy.

Tumor-infiltrating lymphocytes (TILs) are dysfunctional and can be frequently observed in a quiescent state next to growing tumor cells. Nonetheless, the T cells of some patients maintain the capacity to proliferate, persist, and mediate the complete destruction of large tumor deposits (1). This is best illustrated by immunotherapy using immune checkpoint blockade or adoptive cell transfer (ACT), which together represent some of the most important advances in cancer treatment in the past decade (2–5).

The existence of stem cell systems in mature organisms is now well established (6, 7), yet it has been less appreciated that some post-thymic T cells also harbor stem cell–like properties. However, like other adult stem cells in the gut, skin, and olfactory systems, stem cell–like T cells do not function like highly differentiated lymphocytes with regard to the production of effector cytokines and cytotoxicity (8–10). Each T cell specificity (clonotype) can retain key hallmarks of stem cells such as self-renewal, proliferation, and multipotency. For example, TILs can be expanded ex vivo ($>10^{10}$ cells) and readministered to cancer patients, resulting in clonal repopulation and the durable destruction of large metastatic solid tumors (2, 3). We and others have previously identified the transcription factor Tcf7 as being critically involved in the retention of stem cell–like attributes in antigen-experienced T cells (9, 11). Although TILs have historically been thought to be terminally differentiated, TCF7 expression has defined a TIL subset harboring stem cell–like properties (8, 9, 11–15). However, the mechanisms that maintain this TCF7-positive TIL population are minimally understood.

The differentiation of naïve T cells to memory and effector states is largely driven by the strength of the signals they receive, primarily via the T cell receptor (TCR). This maturation process can be subverted by many inhibitory signals that disrupt the signaling cascade after TCR ligation. The progression of T cell differentiation toward full effector function is metabolically driven in part by an anabolic program involving Akt-mTOR (mammalian target of rapamycin) signaling and heritable changes to the epigenetic landscape (16–18). This anabolic metabolism requires the continual uptake and consumption of extracellular nutrients, facilitated by a transmembrane electrochemical gradient present in all living cells (19). Maintenance of this electrochemical gradient involves the monovalent cation potassium, which has an intracellular concentration of ~145 mM, much higher than normally found in the extracellular space (~5 mM).

Despite tumor cell death, a higher density of necrosis is inversely correlated with patient survival in some tumor histologies (20, 21). We previously reported that necrosis leads to a profound alteration of the potassium ion gradient within the tumor microenvironment (TME) (22). Cellular necrosis liberates potassium and other intracellular contents into the extracellular space, which contains the tumor interstitial fluid (TIF). Disrupted tumor vasculature and abnormal lymphatic drainage lead to TIF stasis, causing tumors to be deprived of oxygen and crucial extracellular nutrients, whereas the concentration of TIF potassium remains elevated. The increased extracellular potassium of the TIF acutely suppresses T cell effector function after TCR ligation, limiting T cell activation in a nonredundant manner to both PD-L1 and CTLA-4 immune checkpoints (22). Yet the impact of high levels of extracellular potassium ($\uparrow[K^+]_e$) on nutrient uptake, metabolism, epigenetics, and cellular differentiation has not been explored.

Here, we report experiments in which $\uparrow[K^+]_e$ diminished the uptake and consumption of local nutrients despite adequate extracellular resources, a state we define as functional caloric restriction. Elevated $[K^+]_e$ subsequently triggered a T cell starvation response leading to autophagy, which drove metabolic and epigenetic reprogramming, thereby limiting the acquisition of effector functions and preserving Tcf7 and functional stemness. This epigenetic reprogramming was mediated by the depletion of nucleocytosolic acetyl–coenzyme A (AcCoA). Reductions in available AcCoA decreased histone acetylation, which in turn limited the activation of effector genes. Thus, we find that $\uparrow[K^+]_e$ characteristic of the TME attenuates AcCoA processing, generating antitumor T cells with improved persistence, engraftment, self-renewal, multipotency, and tumor clearance—all characteristics of T cell stemness (23). These data help to resolve the current immunotherapy paradox as to why cancers progress despite the presence of T cells that harbor the capacity for rejuvenation and tumor clearance.

Elevated $[K^+]_e$ triggers functional caloric restriction in T cells

We previously reported that $\uparrow[K^+]_e$ is characteristic of the TME (an additional 40 mM on average) and acutely silences T cell effector function (22), but the impact of $\uparrow[K^+]_e$ on the transmembrane electrochemical gradient and its consequences on T cell nutrient uptake and cellular metabolism remain unclear. We performed comprehensive metabolite analysis using liquid chromatography and mass spectrometry of T cells conditioned in $\uparrow[K^+]_e$ or control media containing ~5 mM K^+. This analysis revealed that $\uparrow[K^+]_e$ exposure resulted in a significant reduction of glycolytic intermediates and essential amino acids within T cells (Fig. 1, A to C, and fig. S1A). These alterations were attributable to a reduction in electrochemically dependent nutrient uptake, because T cells conditioned with $\uparrow[K^+]_e$ or treated with $BaCl_2$, a nonselective inhibitor of potassium channels in the plasma membrane, had diminished uptake of fluorescently labeled glucose and lipid analogs, 2-NBDG and BODIPY FLC_{16}, respectively (Fig. 1, D and E, and fig. S1, B and C). Neither T cell survival nor proliferative potential after restimulation were compromised by $\uparrow[K^+]_e$-mediated reduction of nutrient uptake (fig. S1, D to F). We therefore propose that reduced levels of intracellular anabolic metabolites in the setting of unchanged extracellular nutrient abundance induced by $\uparrow[K^+]_e$ result in a state of functional caloric restriction. These findings are consistent with those of previous studies in nonimmune cells demonstrating that

alterations to the transmembrane potassium concentration and membrane potential (V_{mem}) can attenuate nutrient uptake (24–27) (Fig. 1F).

Although most intracellular metabolites were depressed globally, we noted enrichment in a subset of phospholipid species (Fig. 1G). These included glycerophosphoethanolamine, glycerophosphocholine, phosphoethanolamine, and CDP-ethanolamine (Fig. 1H). These compounds are hallmark metabolites of the Kennedy pathway, a metabolic pathway involved in the de novo biosynthesis of phosphatidylethanolamine (PE), an early initiator of autophagosome fusion and autophagy (Fig. 1I) (28). Analysis of human $CD8^+$ T cells after $\uparrow[K^+]_e$ conditioning also revealed enrichment in Kennedy cycle intermediates (fig. S1G). Additionally, RNA sequencing (RNA-seq) analysis of primary T cells cultured in the presence or absence of $\uparrow[K^+]_e$ demonstrated significant enrichment in autophagy-associated transcripts (Fig. 1J) (29). These data indicated that levels of $\uparrow[K^+]_e$ characteristic of the TME result in a selective accumulation of metabolites required for autophagosome maturation and a gene expression signature indicative of ongoing autophagy.

Functional caloric restriction mediated by increased $[K^+]_e$ promotes autophagy and metabolic reprogramming

To evaluate the impact of $\uparrow[K^+]_e$ on autophagic flux in live T cells, we used an eGFP (enhanced green fluorescent protein)–mCherry-LC3b fusion reporter system (29) (Fig. 2, A and B, and fig. S2A). Microtubule-associated protein I light chain beta (LC3) is hydrolyzed to expose Gly^{120} to create LC3b-I (Fig. 1I). This molecule is in turn conjugated with PE to generate LC3b-II, enabling phagophore expansion to create autophagosomes (30). An autophagy-incompetent construct containing a $Gly^{120} \rightarrow$ Ala substitution (G120A) served as a negative control (fig. S2A). Confocal microscopy demonstrated loss of GFP fluorescence in mCherry puncta in the presence of $\uparrow[K^+]_e$, indicating autophagosome-lysosome fusion (Fig. 2C and fig. S2B). Concurrent flow cytometric analysis confirmed that $\uparrow[K^+]_e$ resulted in a greater proportion of $mCherry^+GFP^-$ cells, suggesting ongoing autophagic flux (Fig. 2D). These dynamic changes in fluorescence were not attributable to artifactual spectral overlap, as the T cell surface marker Thy1.1 was used as an independent validation of transduction, reporter persistence, and increased autophagy in $\uparrow[K^+]_e$-treated cells (fig. S2C).

The relative abundance of the autophagosome proteins LC3b-I and the PE-conjugated form, LC3b-II, were examined by immunoblot. We found that the LC3b-II/LC3b-I ratio was elevated after $\uparrow[K^+]_e$ in both mouse and human T cells, consistent with increased autophagosome formation (Fig. 2, E and F) (30). Collectively, these data demonstrate that antitumor T cells exposed to $\uparrow[K^+]_e$ acquire a metabolic state defined by functional caloric restriction and ongoing autophagy. To investigate whether autophagy induced by $\uparrow[K^+]_e$ was related to a starvation response after depletion of intracellular nutrients, we measured the activity of the Akt-mTOR and AMPK (adenosine monophosphate–activated protein kinase) nutrient-sensing signaling cascades in both mouse and human $CD8^+$ T cells. Increased $\uparrow[K^+]_e$ mediated reduced phosphorylation of Akt (Ser^{473}), mTOR (Ser^{2448}) (fig. S2, D to F), and two modulators of ribosomal activity, S6 ($Ser^{235/6}$) (Fig. 2G and fig. S2, G and H) and 4E-

BP1 ($Thr^{37/46}$) (fig. S2I). Moreover, immunoblot analysis revealed increased activity of the energy sensor AMPK (fig. S2J). Similar findings were observed in human $CD8^+$ T cells, as evidenced by hypophosphorylation of S6 ($Ser^{235/6}$) (Fig. 2H), suggesting induction of nutrient conservation (17).

We next sought to measure the consequences of this starvation response for the metabolic fitness of T lymphocytes expanded in $\uparrow[K^+]_e$ conditions. After $\uparrow[K^+]_e$, T cells exhibited robust mitochondrial function, as evidenced by marked spare respiratory capacity (Fig. 2I). $\uparrow[K^+]_e$ preserved the oxygen consumption capacity of human TILs after reactivation and proliferation, as well as that of TCR-engineered T cells (Fig. 2J and fig. S3A). Consistent with the induction of a mitochondrially dominant program of cellular metabolism, we found that $\uparrow[K^+]_e$-conditioned human $CD8^+$ T cells maintained a lower mitochondrial membrane potential ($\Delta\Psi m$) (fig. S3B). Scanning electron microscopy of T cells expanded in $\uparrow[K^+]_e$ conditions revealed an increase in mitochondrial number and quality (fig. S3C), which suggests that T cells maintained mitochondrial integrity and the capacity for marked on-demand oxygen consumption. From these data, we conclude that cells subjected to $\uparrow[K^+]_e$ had limited ongoing consumption of extracellular energy resources and instead existed in a metabolic state of functional starvation, with a resultant induction in autophagy and mitochondrially driven energy production.

Functional caloric restriction depletes nucleocytosolic AcCoA to suppress effector programs

The enhanced mitochondrial function of T lymphocytes exposed to $\uparrow[K^+]_e$ led us to quantify AcCoA, a molecule that enables carbons derived from carbohydrates, fats, and proteins to be utilized in the citric acid cycle for oxidative phosphorylation. AcCoA also serves as a substrate for histone and non-histone protein acetylation (31, 32). Because the mitochondrial membrane is impermeable to AcCoA, there are two distinct pools of AcCoA in cells: mitochondrial and nucleocytosolic (the latter because cytosolic AcCoA can move freely across the nuclear pore complex) (Fig. 3A) (31). The quantity of AcCoA in the mitochondria is estimated to be several times that in the nucleocytosolic compartment. Thus, total cellular AcCoA is a surrogate for mitochondrial AcCoA (33). In the setting of $\uparrow[K^+]_e$, we observed an elevation in total cellular AcCoA, a finding consistent with mitochondrially oriented metabolism (Fig. 3B).

Despite higher levels of total AcCoA, we measured a reduction in nucleocytosolic AcCoA and its precursor, citrate, in T cells after $\uparrow[K^+]_e$ conditioning (Fig. 3C). These findings, along with a depletion of glycolytic products, suggested preferential generation and utilization of AcCoA within the mitochondria for use in oxidative phosphorylation. To determine the effect of $\uparrow[K^+]_e$ conditioning and consequent depression of nucleocytosolic AcCoA, we measured total acetylated Lys levels in mouse and human T cells (Fig. 3D and fig. S4A). We found a notable reduction in the setting of $\uparrow[K^+]_e$ characteristic of the TME.

The acetylation of histone proteins acts to disrupt DNA-histone salt bridges, allowing for a euchromatin structural organization and increased local gene transcription (34). We sought to assess the potential epigenetic consequences related to the limited nuclear availability of

AcCoA in the setting of ↑$[K^+]_e$. Therefore, we performed chromatin immunoprecipitation and polymerase chain reaction (ChIP-PCR) of acetylated Lys^9 and Lys^{27} of histone H3 (H3K9; H3K27Ac) and found decreased acetylation at both residues for *Ifng* regulatory loci (Fig. 3E). To obtain a whole-genome map of histone acetylation (H3K9Ac) loci and consequent chromatin accessibility, we performed ChIP sequencing (ChIP-seq). We observed reduced acetylation of the promoter and enhancer loci of *Ifng*, as well as loci associated with T cell activation and exhaustion, including *Pdcd1* (PD1), *Cd244* (2B4), *Havcr2* (Tim-3), and *Klrg1* (Fig. 3, F and G, and fig. S4, B and C). We then performed RNA-seq under the same conditions to measure the functional consequences of H3K9 acetylation, with concordant results.

To visualize patterns of changes to H3K9Ac at a whole-genome level, we plotted relative change versus *P* value for differentially acetylated loci of effector genes (Fig. 3H, left, and fig. S5A). We found a notable reduction in activating H3K9Ac histone marks on regulatory elements associated with T cell effector and exhaustion programs. Quantification by gene set enrichment analysis (GSEA) revealed that H3K9Ac acetylation was indeed lost at sites responsible for activation of exhaustion ($Tim3^+$ versus $CXCR5^+$ UP) and effector transcriptional programs (Fig. 3H, right). By contrast, we did not observe differences in H3K9Ac enrichment at constitutively expressed loci in T cells, such as *Cd3e*, *Actb*, or *B2M* (fig. S4, D to G), or differences in total levels of H3K9Ac or H3K27Ac in response to ↑$[K^+]_e$ conditioning (fig. S4H). Our data are consistent with the observation that histone acetyltransferase enzymatic activity and selectivity are modulated by levels of AcCoA. It is likely that existing acetyl groups have higher priority for AcCoA than those involved in the addition of new acetyl groups, like those associated with T cell differentiation (35, 36).

To assess whether H3K9Ac correlated with chromatin accessibility, we compared our observed differential enrichment against a previously reported gene list of effector and exhaustion datasets generated by ATAC-seq analysis in T cells after chronic antigen stimulation (37). We found that H3K9Ac was negatively enriched at loci regulating the transcription of these genes after ↑$[K^+]_e$ (Fig. 3I and fig. S5, B and C). Collectively, these data suggest that ↑$[K^+]_e$ leads to depletion of nucleocytosolic AcCoA, triggering reduced histone acetylation and limiting the epigenetic imprints of effector and exhaustion programs.

Elevated $[K^+]_e$ maintains $CD8^+$ T cell stemness

T cell stemness has generally been defined as the capacity for engraftment, persistence, clonal repopulation, self-renewal, and multipotency, including the capacity for their progeny to acquire typical effector functions such as cytotoxicity and the production of high levels of interferon-γ (IFN-γ) (2, 8, 23). These characteristics exist as a spectrum and coordinately change as T cells mature from naïve to exhausted states (11, 38). Multiple independent preclinical and clinical datasets have identified these “stem-like” features to be highly favorable for cancer immunotherapy in the settings of immune checkpoint blockade and ACT (11, 13, 14). We have previously identified stem cell–like T cells as a subpopulation that has not yet acquired effector programing but expresses the transcription factor Tcf7, the lymphoid homing marker CD62L (Sell, L-selectin), and the costimulatory molecule CD27 (8, 9, 23).

We found that ↑$[K^+]_e$ conditioning triggered functional caloric restriction in T cells, driving a starvation response, thereby altering both cellular metabolism and the epigenetic landscape of effector and stem-associated loci. To understand the impact of ↑$[K^+]_e$ on the function and phenotype of antitumor T cells, we performed RNA-seq and found that the mRNAs for key markers of T cell memory formation and stemness, including *Bach2*, *Il7r*, *Bcl6*, and *Klf2*, were comparatively enriched after exposure to ↑$[K^+]_e$ (Fig. 4A). GSEA revealed that ↑$[K^+]_e$ conditioning resulted in a transcriptional profile that parallels the subset of $CD8^+$ T cells recently identified as retaining stemness and the capacity to respond to PD-1 therapy in the setting of chronic antigen exposure (15) (Fig. 4B).

T cell conditioning in ↑$[K^+]_e$ thus had the dual effect of reducing chromatin activation and gene expression of T cell effector functions and preserving a T cell gene signature with augmented stemness. This was confirmed by quantifying the preservation of Tcf7 transcript and protein (Fig. 4C and fig. S5D). We found that $CD8^+$ T cells exposed to ↑$[K^+]_e$ characteristic of the TME or treated with $BaCl_2$ maintained relatively higher expression of the lymphoid homing marker CD62L (Fig. 4D and fig. S5, E and F) and the costimulatory marker CD27 (Fig. 4E) and retained the capacity to robustly produce interleukin-2 (IL-2) (fig. S5, G and H). These changes were coincident with reduced acquisition of effector function, expression of co-inhibitory surface markers, and the acute suppression of T cell target cytolysis (fig. S5, I to K). ↑$[K^+]_e$ conditioning also delayed the acquisition of effector function even after robust T cell priming (fig. S5L).

To understand the epigenetic basis underlying the sustained expression of stemness genes, we further examined chromatin structure by measuring trimethylation of Lys^{27} on histone H3 (H3K27me3), which recruits the polycomb repressive complex with subsequent compaction of chromatin and suppression of transcription. Metabolite analysis after ↑$[K^+]_e$ revealed depletion of methionine and members of the methionine cycle, including *S*-adenosylmethionine (SAM) and *S*-adenosylhomocysteine (SAH) (Fig. 1C and fig. S6A), without significant effect on the total abundance of H3K27me3 (fig. S6B). To evaluate the impact on histone methylation and cellular function, we assessed H3K27me3 deposition by ChIP-seq. Comparative analysis of whole-genome H3K27me3 enrichment revealed a lack of these repressive marks at the regulatory loci of stemness-defining transcription factors, including *Bach2*, *Tcf7*, *Klf2*, and *Id3* (fig. S6C). Consistent with ↑$[K^+]_e$-mediated disruption of methionine abundance driving epigenetic preservation of T cell stemness, we found an inverse enrichment for H3K27me3 repression within naïve associated genes (fig. S6, D and E). These findings indicate that ↑$[K^+]_e$ depletes metabolites required for suppression of stemness-associated loci during T cell differentiation (39). We found that ionic control of metabolic and epigenetic programs was specific to changes in extracellular potassium, because changes to sodium concentration, tonicity, and inert osmolytes did not have a similar effect on T cell phenotype (fig. S6, F and G). The modulatory effects of ↑$[K^+]_e$ were not restricted to $CD8^+$ T cells, and acquisition of effector programs was similarly delayed in $CD4^+$ T cells, with decreased IFN-γ and preserved IL-2 production in the setting of ↑$[K^+]_e$ (fig. S7, A to C).

Given the impact of conditioning T cells in ↑$[K^+]_e$ on chromatin structure and gene expression, we sought to measure its impact on clinically relevant human tumor-specific T

cells, especially those specific for neoantigens. We therefore obtained tumor-infiltrating T cells isolated from patient tumors and expanded them in the presence or absence of $\uparrow[K^+]_e$. Tumor samples from patients with diverse cancers including melanoma and other solid cancers of the colon, lung, and ovary were subjected to whole-exome sequencing to identify nonsynonymous mutations that result in the creation of potential neoantigens. The precise antigens recognized by each patient's TIL were identified (table S1). We measured increases in the percentages of cells expressing CD62L in these human TILs (Fig. 4, F and G, fig. S7D, and table S1). These findings were surprising, given that these T cell clonotypes had likely been chronically exposed to antigen.

To evaluate the effects of $\uparrow[K^+]_e$ on antitumor T cell function in vivo, we used the adoptive transfer of pmel T cells after activation in $\uparrow[K^+]_e$ to treat mice bearing established B16 melanoma. We found that conditioning with $\uparrow[K^+]_e$ improved T cell persistence after adoptive transfer within secondary lymphoid organs and the tumor site (fig. S8, A to C). Furthermore, antitumor T cells exposed to $\uparrow[K^+]_e$ harbored retained multipotency, demonstrating a comparatively less differentiated state ($CXCR5^+Tim3^-$) within the tumor and spleen after adoptive transfer (Fig. 4H and fig. S8, D and E) and maintaining higher autophagic flux (fig. S8, F and G). Both tumor regression and survival were significantly improved in mice receiving $\uparrow[K^+]_e$-conditioned $CD8^+$ T cells (Fig. 4I). Similar results were also observed in $\uparrow[K^+]_e$-conditioned antitumor $CD4^+$ T cells (fig. S9F).

To further assess the capacity of $\uparrow[K^+]_e$-conditioned T cells to retain the epigenetic imprint of stemness in vivo, we re-isolated $CD90.1^+$ TILs from established tumors and retransferred them to separately congenically distinguishable $CD90.2^+$ hosts with concurrent antigen-specific vaccination. We found that $\uparrow[K^+]_e$-conditioned T cells harbored greater capacity for recall response to antigen (Fig. 4J), were maintained at a comparatively less differentiated state, and displayed greater persistence and self-renewal after antigen rechallenge (fig. S9, A to E). We surmise that $\uparrow[K^+]_e$ mediates a preservation of cellular function and phenotype characteristic of T cell stemness despite exposure to the dysregulatory environment of the TME.

Increased $[K^+]_e$ preserves stemness by mediating AcCoA abundance and autophagy

T cells conditioned by $\uparrow[K^+]_e$ experienced a starvation response that resulted in the lack of acquisition of effector function and the preservation of stemness. Although this provides correlation between these changes and the depression of nucleocytosolic AcCoA, we sought to determine whether these associations were causal. To this end, we supplemented T cells with exogenous acetate, the immediate precursor of AcCoA, or directly electroporated AcCoA into $\uparrow[K^+]_e$-treated cells (40, 41). We confirmed that these interventions restored nucleocytosolic AcCoA (Fig. 5A) and subsequently observed a reduction in CD62L expression (Fig. 5, B and C) and autophagy (Fig. 5D) in the setting of $\uparrow[K^+]_e$. Similarly, AcCoA or acetate provision restored T cell IFN-γ production despite prior conditioning with $\uparrow[K^+]_e$ (Fig. 5, E and F, and fig. S10, A and B). Thus, supplementation of AcCoA

functionally reversed T cell autophagy and stemness programs, enabling the acquisition of effector programs that are otherwise suppressed by conditioning T cells in ↑$[K^+]_e$.

To examine whether these changes had an epigenetic basis, we provided acetate to T cells expanded under ↑$[K^+]_e$ conditions and measured H3K9Ac at the *Ifng* promoter and *Pdcd1* enhancer loci (Fig. 5G). We found that provision of acetate enabled acetylation of these hallmark chromatin sites associated with effector and exhaustion programs. We also clearly visualized that CD62L, a phenotypic marker of stemness, was lost upon electroporation of AcCoA. These findings reflect the capacity for AcCoA replenishment to restore effector programs across multiple time points collected throughout T cell activation (fig. S10, C to H). Thus, this metabolic intervention enabled the liberation of an effector phenotype in T cells grown under the influence of ↑$[K^+]_e$ conditioning, regardless of prior priming. Furthermore, these results indicated that restoration of AcCoA was sufficient to normalize histone acetylation of effector programs even in conditions of ↑$[K^+]_e$.

To assess the causal relationship between T cell differentiation and AcCoA abundance, we used alternate means to manipulate AcCoA levels. Nucleocytosolic AcCoA can be generated by the conversion of citrate to AcCoA and oxaloacetate by the enzyme ATP citrate lyase (ACLY) (Fig. 5H). The compound 2-hydroxycitrate (2-HC) inhibits ACLY, resulting in reduced nucleocytosolic AcCoA (42). We found that T cell exposure to 5 mM 2-HC induced accumulation of cytoplasmic citrate and depleted nucleocytosolic AcCoA (Fig. 5, H and I). Similar to ↑$[K^+]_e$ conditioning, 2-HC reduced $CD8^+$ T cell H3K9Ac enrichment at the *Ifng* promoter (Fig. 5,J and K), increased CD62L surface expression, enhanced autophagic flux, and limited apoptosis and the acquisition of effector programs without compromise to cellular expansion (fig. S11, A to G). Provision of exogenous acetate in the setting of 2-HC treatment again restored IFN-γ production and ablated markers of autophagy (Fig. 5L and fig. S12, A to D), indicating that modulation of AcCoA abundance that does not involve ↑$[K^+]_e$ can act primarily to determine T cell fate and function.

The impact of 2-HC on T cell persistence in vivo was assessed by adoptively transferring congenically marked pmel TCR transgenic $CD8^+$ T cells treated with 2-HC and challenging the mice with vaccinia virus expressing hgp100. An increased persistence of 2-HC–treated cells was found 7 days after ACT, in comparison to control conditions (Fig. 5M and fig. S12E). After ACT for the treatment of both large established subcutaneous tumors and pulmonary metastases, 2-HC treatment of pmel T cells resulted in improved tumor treatment and host survival (Fig. 5, N and O, and fig. S12F). These data demonstrate that multiple independent routes for attenuating AcCoA abundance have common epigenetic and metabolic mechanisms that can determine T cell function.

These findings led us to further examine the role of autophagy across T cell differentiation states. We observed that after ↑$[K^+]_e$, those cells that harbored ongoing autophagy were more likely to express CD62L (Fig. 5P). To directly address whether intact autophagy was a requirement for T cell stemness after ↑$[K^+]_e$ conditioning of T cells, we employed CRISPR/Cas9-mediated disruption of the *Atg7* locus, a gene obligate for intact autophagy (29). We generated multiple single guide RNAs for this purpose and validated their disruption of Atg7 at the protein level (fig. S13, A and B). We found that after Atg7 knockout (KO), ↑$[K^+]_e$

failed to enrich CD62L surface expression, indicating that autophagy was indeed required for retained stemness in this setting (Fig. 5Q and fig. S13C). Taken together, these data support a mechanistic relationship among autophagy, AcCoA metabolism, and ↑$[K^+]_e$-mediated retention of stemness and suggest that the capacity for metabolic reprogramming is a prerequisite for $CD8^+$ T cell response to ↑$[K^+]_e$.

Increased $[K^+]_e$ promotes selective induction of mitochondrial AcCoA synthetase 1 (Acss1)

Enzymes responsible for AcCoA metabolism in the mitochondria and cytoplasm include acyl-CoA synthetase short-chain family members Acss1 and Acss2 (Fig. 6A). Prior investigations have found these enzymes to be induced under nutrient restriction as a starvation response, allowing for enhanced conversion of acetate to AcCoA to support cell survival (41, 43). Given our prior findings, we sought to delineate changes in these enzymes after exposure to ↑$[K^+]_e$. Although we found that transcripts for both enzymes were higher under ↑$[K^+]_e$ conditioning, protein levels were elevated only for Acss1 (Fig. 6, B and C).

We investigated whether expression of *Acss1* or *Acss2* could mediate metabolic reprogramming, and found that enforced expression of Acss1, but not Acss2, enhanced $CD8^+$ T cell basal and maximal oxygen consumption (Fig. 6D), consistent with the view that ↑$[K^+]_e$ induces mitochondrially oriented metabolism. On the basis of these observations, we explored whether Acss1 could metabolically reprogram T cells, including those used in therapeutic settings. We retrovirally transduced tumor-reactive $CD8^+$ T cells to enable their constitutive expression of Acss1, and confirmed its localization to mitochondria (Fig. 6E). Metabolite analysis of *Acss1*-overexpressing cells revealed an increase in mitochondrial AcCoA (as measured by total cellular AcCoA) without any differences in nucleocytosolic AcCoA or cytoplasmic citrate levels (fig. S13, D and E). We observed increased autophagic flux upon enforced expression of Acss1 (Fig. 6F) as well as reduced p4E-BP1 and pS6 in cells overexpressing Acss1 (Fig. 6, G and H). Our findings are consistent with Acss1 induction of autophagic flux and mitochondrially oriented metabolism, the metabolic features of memory T cells.

Because enforced expression of Acss1 resembled ↑$[K^+]_e$-conditioned T cells in many respects, we sought to probe their function in vivo. We found that $CD8^+$ T cells engineered to express Acss1 demonstrated markedly improved persistence after viral infection (fig. S13F). Most important, we found that pmel $CD8^+$ T cells engineered to express Acss1 mediated improved tumor treatment and survival of mice bearing established B16 tumors (Fig. 6I). Taken together, these data show that the Acss1 protein is enriched upon nutrient restriction induced by ↑$[K^+]_e$ and that enforced expression of Acss1 can metabolically reprogram antitumor T cells by driving enhanced oxygen utilization and autophagy (Fig. 6J), improving T cell persistence as well as tumor clearance and survival in tumor-bearing mice.

Conclusions

T cells are subject to persistent antigen exposure within tumors, resulting in continual TCR signaling and progressive cellular differentiation. Despite these forces driving T cell

exhaustion, some TIL populations retain stemness and harbor the capacity to mediate tumor clearance. The stemness of TILs is perhaps most evident after immune checkpoint blockade or the reinfusion of ex vivo expanded TILs, but the mechanisms underlying this phenotypic and functional TIL reserve were previously poorly understood. Here, we report that $\uparrow[K^+]_e$ characteristic of the TME limits T cell effector function and preserves T cell stemness.

We propose a model whereby alterations in nutrient processing and metabolism act to epigenetically regulate gene transcription and T cell stemness (fig. S14). Ultimately, the subcellular abundance of AcCoA determines T cell phenotype and function. Our finding that Acss1 was induced in the setting of $\uparrow[K^+]_e$ is consistent with reports indicating that acetate becomes a major carbon source for metabolism during the starvation response, leading to reduced posttranslational acetylation of proteins including histones. We discovered that provision of supplemental acetate under conditions of $\uparrow[K^+]_e$ rescues the epigenetic program of T cell function, a finding consistent with previous reports that acetate restores the function of $CD8^+$ T cells induced by stress responses after acute bacterial infection (Fig. 5, A to G, and fig. S10, A to H) (41). These findings parallel recent reports that demonstrate the cellular need for available AcCoA to enact epigenetic maturation during a starvation response (44).

Our data support intervention and reprogramming of the metabolic state as a strategy to improve T cell–based immunotherapy for cancer. These findings identify potential manipulations of T cells via reversible ex vivo means as well as durable genetic intervention to improve antitumor function. Our work additionally provides insights into the dynamic interplay between tumor-induced suppression of T cell effector function and its coincident influence upon stemness.

Supplementary Material

Refer to Web version on PubMed Central for supplementary material.

ACKNOWLEDGMENTS

We thank S. A. Rosenberg for valuable discussions and intellectual input, A. Mixon and S. Farid for expertise with cell sorting, G. McMullen and D. Jones for expertise with mouse handling, F. Soheilian and N. de Val (NCI Leidos core) for electron microscopy, D.-Y. Lee (NHLBI Biochemistry core) for help related to AcCoA measurements, and J. Shetty and B. Tran of the NCI Sequencing Facility.

Funding:

Supported by the Intramural Research Program of the NCI, the Cancer Moonshot Program for the Center for Cell-Based Therapy at the NCI, NIH, and the Milstein Family Foundation.

REFERENCES AND NOTES

1. Rosenberg SA, Restifo NP, Adoptive cell transfer as personalized immunotherapy for human cancer. Science 348, 62–68 (2015). doi: 10.1126/science.aaa4967; pmid: 25838374 [PubMed: 25838374]
2. Dudley ME et al., Cancer regression and autoimmunity in patients after clonal repopulation with antitumor lymphocytes. Science 298, 850–854 (2002). doi: 10.1126/science.1076514; pmid: 12242449 [PubMed: 12242449]

3. Rosenberg SA et al., Durable complete responses in heavily pretreated patients with metastatic melanoma using T-cell transfer immunotherapy. Clin. Cancer Res 17, 4550–4557 (2011). doi: 10.1158/1078-0432.CCR-11-0116; pmid: 21498393 [PubMed: 21498393]
4. Zacharakis N et al., Immune recognition of somatic mutations leading to complete durable regression in metastatic breast cancer. Nat. Med 24, 724–730 (2018). doi: 10.1038/s41591-018-0040-8; pmid: 29867227 [PubMed: 29867227]
5. Ribas A, Wolchok JD, Cancer immunotherapy using checkpoint blockade. Science 359, 1350–1355 (2018). doi: 10.1126/science.aar4060; pmid: 29567705 [PubMed: 29567705]
6. Naik S, Larsen SB, Cowley CJ, Fuchs E, Two to Tango: Dialog between Immunity and Stem Cells in Health and Disease. Cell 175, 908–920 (2018). doi: 10.1016/j.cell.2018.08.071; pmid: 30388451 [PubMed: 30388451]
7. Gehart H, Clevers H, Tales from the crypt: New insights into intestinal stem cells. Nat. Rev. Gastroenterol. Hepatol 16, 19–34 (2019). doi: 10.1038/s41575-018-0081-y; pmid: 30429586 [PubMed: 30429586]
8. Gattinoni L et al., Wnt signaling arrests effector T cell differentiation and generates CD8+ memory stem cells. Nat. Med 15, 808–813 (2009). doi: 10.1038/nm.1982; pmid: 19525962 [PubMed: 19525962]
9. Gattinoni L et al., A human memory T cell subset with stem cell-like properties. Nat. Med. 17, 1290–1297 (2011). doi: 10.1038/nm.2446; pmid: 21926977 [PubMed: 21926977]
10. Restifo NP, Gattinoni L, Lineage relationship of effector and memory T cells. Curr. Opin. Immunol 25, 556–563 (2013). doi: 10.1016/j.coi.2013.09.003; pmid: 24148236 [PubMed: 24148236]
11. Sade-Feldman M et al., Defining T Cell States Associated with Response to Checkpoint Immunotherapy in Melanoma. Cell 175, 998–1013.e20 (2018). doi: 10.1016/j.cell.2018.10.038; pmid: 30388456 [PubMed: 30388456]
12. Philip M et al., Chromatin states define tumour-specific T cell dysfunction and reprogramming. Nature 545, 452–456 (2017). doi: 10.1038/nature22367; pmid: 28514453 [PubMed: 28514453]
13. Kurtulus S et al., Checkpoint Blockade Immunotherapy Induces Dynamic Changes in PD-1−CD8+ Tumor-Infiltrating T Cells. Immunity 50, 181–194.e6 (2019). doi: 10.1016/j.immuni.2018.11.014; pmid: 30635236 [PubMed: 30635236]
14. Siddiqui I et al., Intratumoral Tcf1+PD-1+CD8+ T Cells with Stem-like Properties Promote Tumor Control in Response to Vaccination and Checkpoint Blockade Immunotherapy. Immunity 50, 195–211.e10 (2019). doi: 10.1016/j.immuni.2018.12.021; pmid: 30635237 [PubMed: 30635237]
15. Im SJ et al., Defining CD8+ T cells that provide the proliferative burst after PD-1 therapy. Nature 537, 417–421 (2016). doi: 10.1038/nature19330; pmid: 27501248 [PubMed: 27501248]
16. Crompton JG et al., Lineage relationship of CD8+ T cell subsets is revealed by progressive changes in the epigenetic landscape. Cell. Mol. Immunol 13, 502–513 (2016). doi: 10.1038/cmi.2015.32; pmid: 25914936 [PubMed: 25914936]
17. Chi H, Regulation and function of mTOR signalling in T cell fate decisions. Nat. Rev. Immunol 12, 325–338 (2012). doi: 10.1038/nri3198; pmid: 22517423 [PubMed: 22517423]
18. Kishton RJ, Sukumar M, Restifo NP, Metabolic Regulation of T Cell Longevity and Function in Tumor Immunotherapy. Cell Metab 26, 94–109 (2017). doi: 10.1016/j.cmet.2017.06.016; pmid: 28683298 [PubMed: 28683298]
19. Lodish H, Berk A, Zipursky S, in Molecular Cell Biology, 4th Edition (2000), pp. 1–5.
20. Ladstein RG, Bachmann IM, Straume O, Akslen LA, Tumor necrosis is a prognostic factor in thick cutaneous melanoma. Am. J. Surg. Pathol 36, 1477–1482 (2012). doi: 10.1097/PAS.0b013e31825a5b45; pmid: 22982891 [PubMed: 22982891]
21. Komori K et al., Tumor necrosis in patients with TNM stage IV colorectal cancer without residual disease (R0 Status) is associated with a poor prognosis. Anticancer Res 33, 1099–1105 (2013). pmid: 23482787 [PubMed: 23482787]
22. Eil R et al., Ionic immune suppression within the tumour microenvironment limits T cell effector function. Nature 537, 539–543 (2016). doi: 10.1038/nature19364; pmid: 27626381 [PubMed: 27626381]

23. Gattinoni L, Klebanoff CA, Restifo NP, Paths to stemness: Building the ultimate antitumour T cell. Nat. Rev. Cancer 12, 671–684 (2012). doi: 10.1038/nrc3322; pmid: 22996603 [PubMed: 22996603]
24. Schafer JA, Heinz E, The effect of reversal on Na+ and K+ electrochemical potential gradients on the active transport of amino acids in Ehrlich ascites tumor cells. Biochim. Biophys. Acta 249, 15–33 (1971). doi: 10.1016/0005-2736(71)90079-4; pmid: 5141124 [PubMed: 5141124]
25. Eddy AA, Mulcahy MF, Thomson PJ, The effects of sodium ions and potassium ions on glycine uptake by mouse ascites-tumour cells in the presence and absence of selected metabolic inhibitors. Biochem. J 103, 863–876 (1967). doi: 10.1042/bj1030863; pmid: 6072273 [PubMed: 6072273]
26. Cummins CJ, Glover RA, Sellinger OZ, Potassium modulation of methionine uptake in astrocytes in vitro. Neurochem. Res 7, 637–644 (1982). doi: 10.1007/BF00965129; pmid: 7121715 [PubMed: 7121715]
27. Levite M et al., Extracellular K+ and opening of voltagegated potassium channels activate T cell integrin function: Physical and functional association between Kv1.3 channels and beta1 integrins. J. Exp. Med 191, 1167–1176 (2000). doi: 10.1084/jem.191.7.1167; pmid: 10748234 [PubMed: 10748234]
28. Gibellini F, Smith TK, The Kennedy pathway—De novo synthesis of phosphatidylethanolamine and phosphatidylcholine. IUBMB Life 62, 414–428 (2010). doi: 10.1002/iub.354; pmid: 20503434 [PubMed: 20503434]
29. Xu X et al., Autophagy is essential for effector CD8+ T cell survival and memory formation. Nat. Immunol 15, 1152–1161 (2014). doi: 10.1038/ni.3025; pmid: 25362489 [PubMed: 25362489]
30. Klionsky DJ et al., Guidelines for the use and interpretation of assays for monitoring autophagy. Autophagy 12, 1–222 (2012). doi: 10.4161/auto.19496; pmid: 26799652
31. Pietrocola F, Galluzzi L, Bravo-San Pedro JM, Madeo F, Kroemer G, Acetyl coenzyme A: A central metabolite and second messenger. Cell Metab 21, 805–821 (2015). doi: 10.1016/j.cmet.2015.05.014; pmid: 26039447 [PubMed: 26039447]
32. Menzies KJ, Zhang H, Katsyuba E, Auwerx J, Protein acetylation in metabolism - metabolites and cofactors. Nat. Rev. Endocrinol 12, 43–60 (2016). doi: 10.1038/nrendo.2015.181; pmid: 26503676 [PubMed: 26503676]
33. Weinert BT et al., Acetylation dynamics and stoichiometry in Saccharomyces cerevisiae. Mol. Syst. Biol 10, 716 (2014). doi: 10.1002/msb.134766; pmid: 24489116 [PubMed: 24489116]
34. Drazic A, Myklebust LM, Ree R, Arnesen T, The world of protein acetylation. Biochim. Biophys. Acta 1864, 1372–1401 (2016). doi: 10.1016/j.bbapap.2016.06.007; pmid: 27296530 [PubMed: 27296530]
35. Denisov IG, Sligar SG, A novel type of allosteric regulation: Functional cooperativity in monomeric proteins. Arch. Biochem. Biophys 519, 91–102 (2012). doi: 10.1016/j.abb.2011.12.017; pmid: 22245335 [PubMed: 22245335]
36. Henry RA, Kuo Y-MM, Bhattacharjee V, Yen TJ, Andrews AJ, Changing the selectivity of p300 by acetyl-CoA modulation of histone acetylation. ACS Chem. Biol 10, 146–156 (2015). doi: 10.1021/cb500726b; pmid: 25325435 [PubMed: 25325435]
37. Pauken KE et al., Epigenetic stability of exhausted T cells limits durability of reinvigoration by PD-1 blockade. Science 354, 1160–1165 (2016). doi: 10.1126/science.aaf2807; pmid: 27789795 [PubMed: 27789795]
38. Azizi E et al., Single-Cell Map of Diverse Immune Phenotypes in the Breast Tumor Microenvironment. Cell 174, 1293–1308.e36 (2018). doi: 10.1016/j.cell.2018.05.060; pmid: 29961579 [PubMed: 29961579]
39. Gray SM, Amezquita RA, Guan T, Kleinstein SH, Kaech SM, Polycomb Repressive Complex 2-Mediated Chromatin Repression Guides Effector CD8+ T Cell Terminal Differentiation and Loss of Multipotency. Immunity 46, 596–608 (2017). doi: 10.1016/j.immuni.2017.03.012; pmid: 28410989 [PubMed: 28410989]
40. Peng M et al., Aerobic glycolysis promotes T helper 1 cell differentiation through an epigenetic mechanism. Science 354, 481–484 (2016). doi: 10.1126/science.aaf6284; pmid: 27708054 [PubMed: 27708054]

41. Balmer MLL et al., Memory CD8+ T Cells Require Increased Concentrations of Acetate Induced by Stress for Optimal Function. Immunity 44, 1312–1324 (2016). doi: 10.1016/j.immuni.2016.03.016; pmid: 27212436 [PubMed: 27212436]

42. Pietrocola F et al., Caloric Restriction Mimetics Enhance Anticancer Immunosurveillance. Cancer Cell 30, 147–160 (2016). doi: 10.1016/j.ccell.2016.05.016; pmid: 27411589 [PubMed: 27411589]

43. Lakhter AJ et al., Glucose-independent Acetate Metabolism Promotes Melanoma Cell Survival and Tumor Growth. J. Biol. Chem 291, 21869–21879 (2016). doi: 10.1074/jbc.M115.712166; pmid: 27539851 [PubMed: 27539851]

44. Liu X et al., Acetate Production from Glucose and Coupling to Mitochondrial Metabolism in Mammals. Cell 175, 502–513.e13 (2018). doi: 10.1016/j.cell.2018.08.040; pmid: 30245009 [PubMed: 30245009]

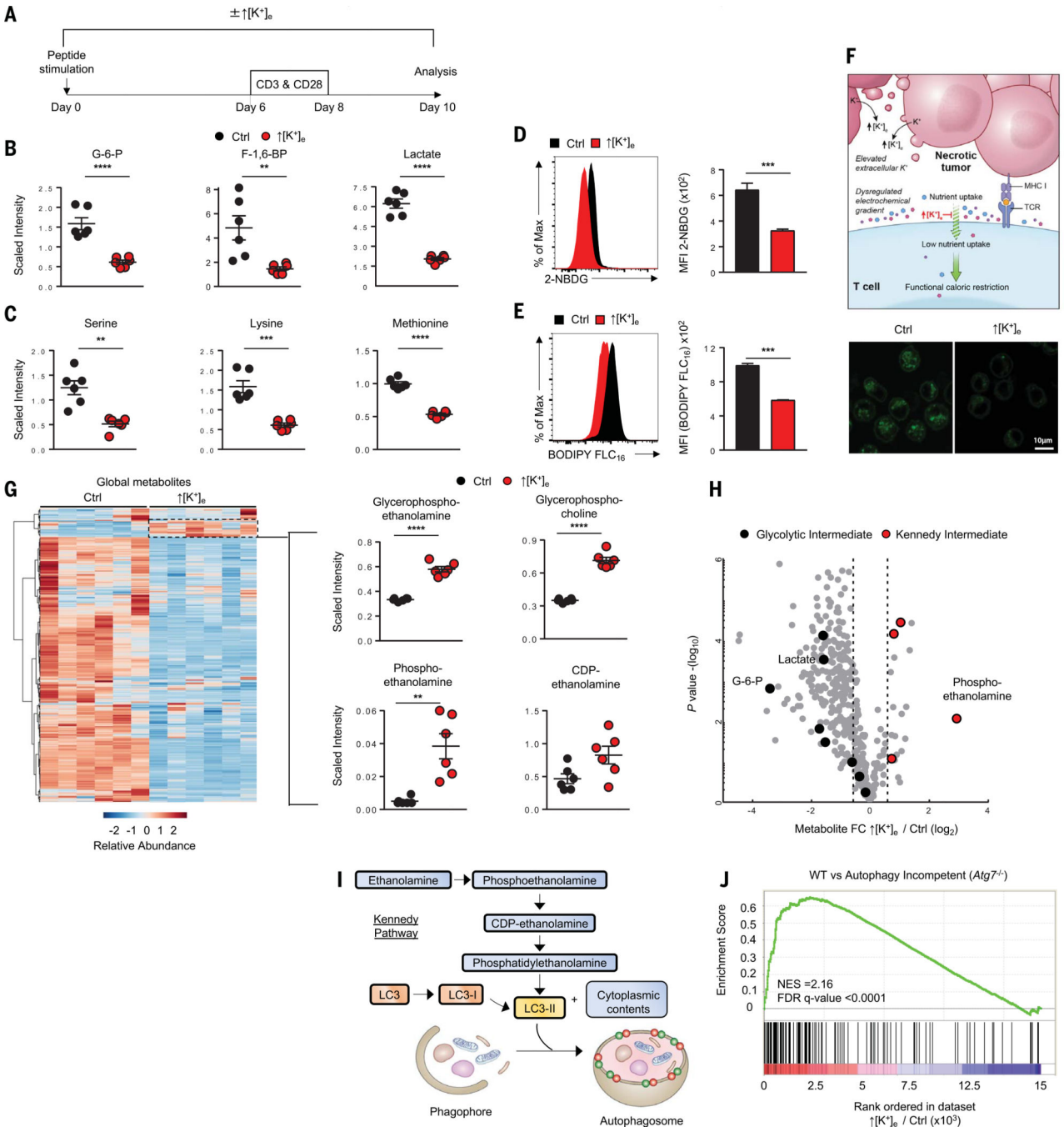

Fig. 1. Increased $[K^+]_e$ limits nutrient uptake and triggers functional caloric restriction in T cells.

(**A**) Experimental setup for activation of $CD8^+$ T cells in the indicated conditions: control (regular media; 5 mM K^+) or $\uparrow[K^+]_e$ (an additional 40 mM K^+). (**B** and **C**) Quantification of glycolysis metabolites (B) and amino acids (C) by liquid chromatography and mass spectrometry in the indicated conditions (data shown are means ± SEM of six replicates per condition). (**D**) 2-NBDG uptake in the indicated conditions with representative histograms and quantification. (**E**) Representative fluorescence-activated cell sorting (FACS) histogram,

quantification, and confocal images showing reduced BODIPY FLC_{16} uptake in $\uparrow[K^+]_e$ versus control T cells. In (D) and (E), values indicate average geometric mean fluorescence intensity; data are means ± SEM and are representative of two independent experiments. See fig. S1B for confocal quantifications. (**F**) Schematic of necrotic tumors (pink) liberating intracellular potassium into the tumor interstitial fluid. This disrupts the electrochemical gradient and limits the ability of T cells to take up nutrients (blue, purple, and red symbols), resulting in functional caloric restriction. (**G**) Left: Heat map shows relative abundance of profiled metabolites in T cells under control and $\uparrow[K^+]_e$ conditions. Right: Quantifications highlight the subset of lipid species enriched involving autophagy flux. Data are means ± SEM of six replicates per conditionper condition. (**H**) Volcano plot representing decreased glycolysis metabolites (black) and enrichment of Kennedy intermediates (red). Metabolite abundance is represented as relative change (*x* axis) versus significance (*y* axis). (**I**) Schematic of the molecular pathways involved in autophagy and the role of Kennedy pathway components in LC3 lipidation for phagophore formation. (**J**) GSEA of $\uparrow[K^+]_e$ versus control transcriptional profile compared with wild-type versus Atg7 KO datasets (GSE57047). NES, normalized enrichment score. All metabolomic data are means ± SEM of six replicates per condition. $^{**}P < 0.01$, $^{***}P < 0.001$, $^{****}P < 0.0001$ (two-tailed *t* tests).

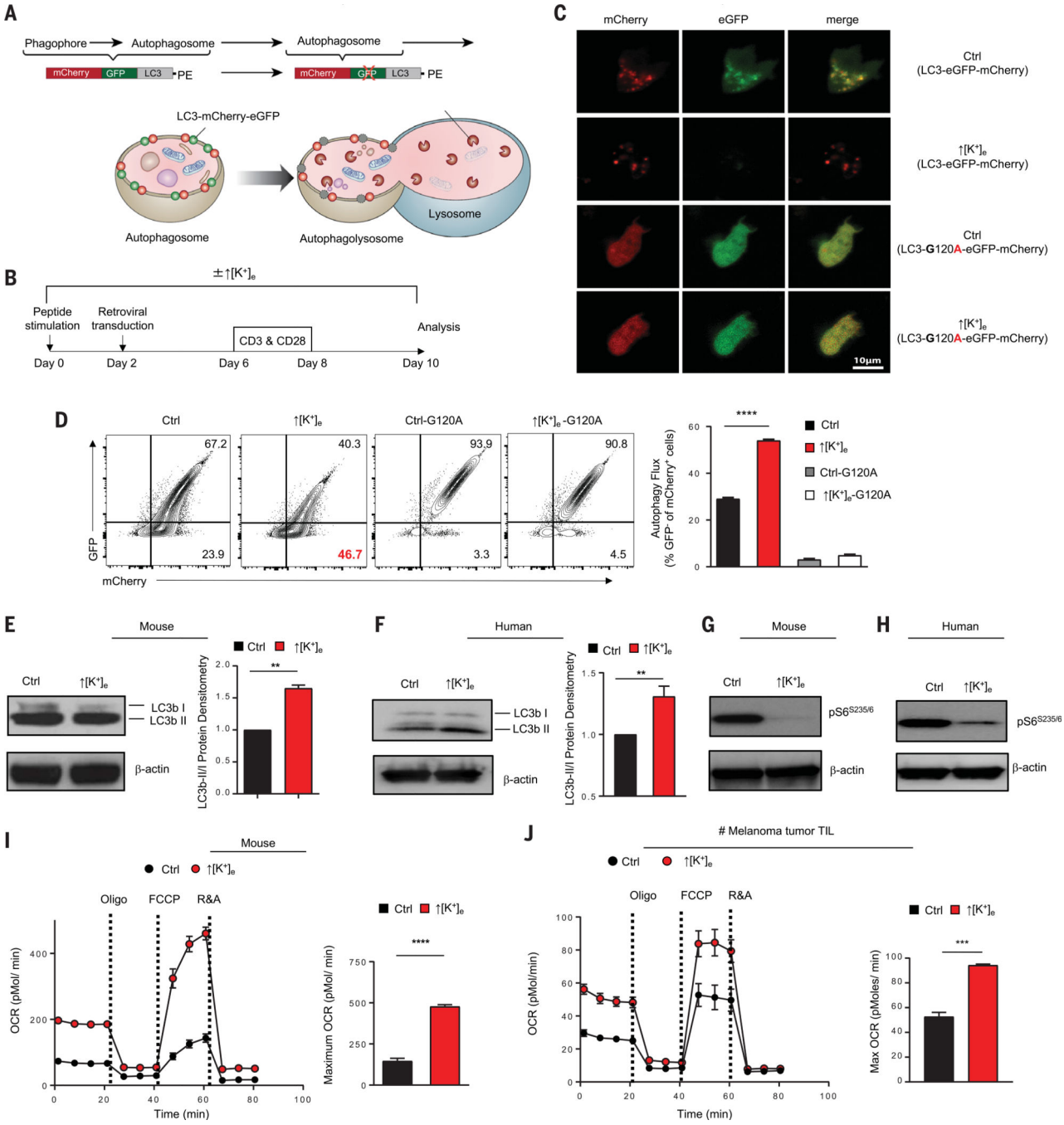

Fig. 2. T cells exposed to increased $[K^+]_e$ recycle nutrients via autophagy during functional caloric restriction.

(**A**) Schematic for monitoring autophagy flux using retroviral mCherry-eGFP-LC3 construct. (**B**) Experimental setup of in vitro culture conditions for activation of pmel $CD8^+$ T cells with gp100, followed by retroviral transduction with mCherry-GFP-LC3 construct at indicated time points. (**C**) Representative live-cell confocal images defining the GFP and mCherry puncta in cells treated under the indicated conditions. See fig. S2B for quantification of confocal images. (**D**) Representative flow cytometry plot and quantification

of autophagy flux in the indicated conditions by measuring the loss of GFP in mCherry populations. Data are means ± SEM and are representative of two independent experiments. (**E** and **F**) Immunoblot densitometries and quantification of mouse or human $CD8^+$ Tcells for LC3b-I and LC3b-II in control or $\uparrow[K^+]_e$ conditions. Quantification of autophagy flux is represented by ratio of LCb3-II/LC3b-I intensities. Data are means ± SEM of three independent Western blots. (**G** and **H**) Immunoblot densitometry of $CD8^+$ Tcells obtained from mouse or human for phosphor-S6 ($Ser^{235/236}$) in control or $\uparrow[K^+]_e$ conditions. (**I** and **J**) Representative O_2 consumption rates (OCR) of $CD8^+$ pmel transgenic Tcells and $CD8^+$ T cells obtained from fresh tumor digest of a melanoma patient cultured in control or $\uparrow[K^+]_e$ measured in real time under basal conditions in response to the mitochondrial inhibitors oligomycin, FCCP [carbonyl cyanide 4-(trifluoromethoxy)phenylhydrazone], and R&A (rotenone and antimycin). For all relevant panels here and in later figures, center values and error bars represent means ± SEM. $^{**}P < 0.01$, $^{***}P < 0.001$, $^{****}P < 0.0001$ (two-tailed *t* tests).

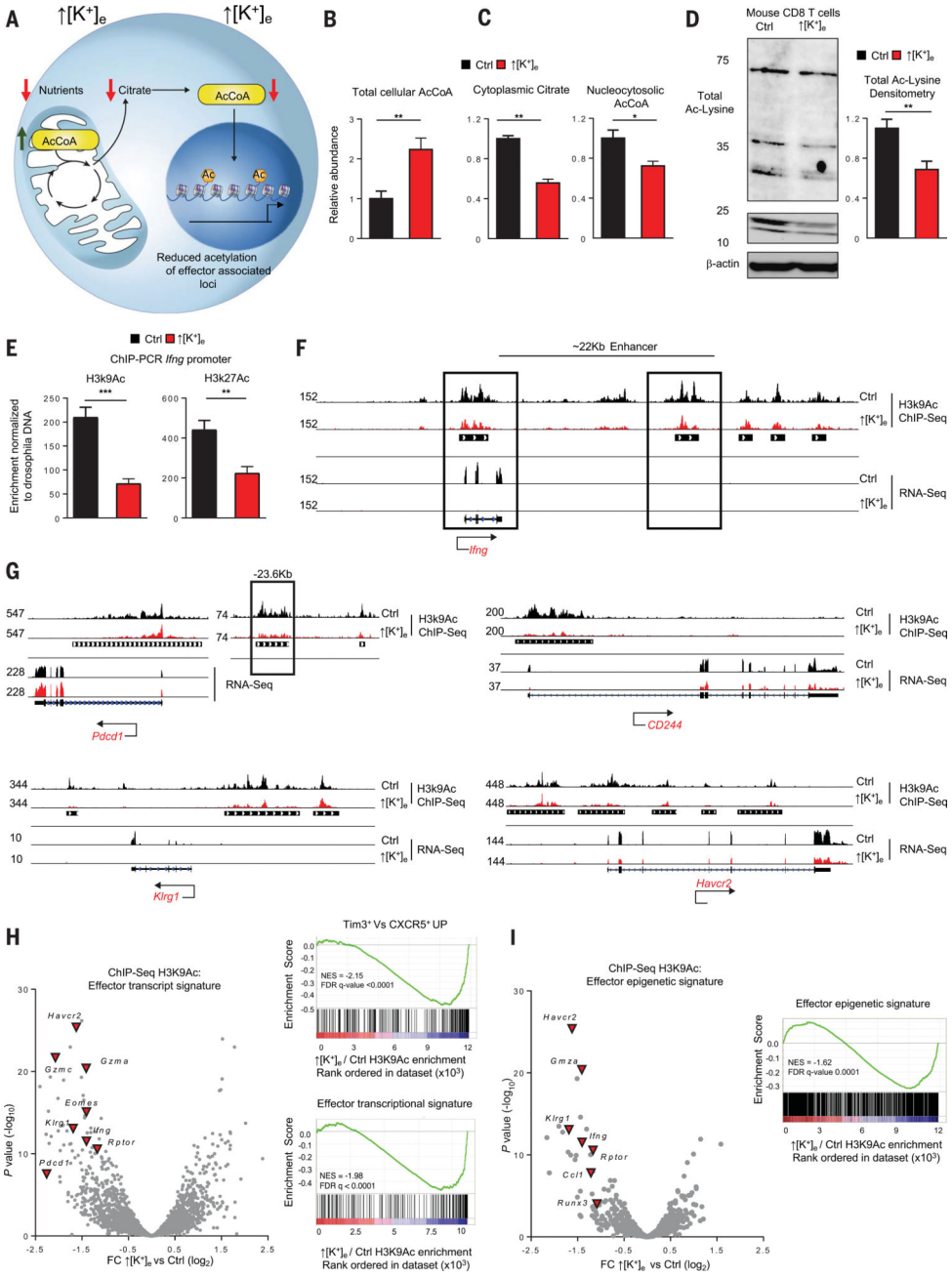

Fig. 3. Elevated $[K^+]_e$-mediated metabolic programming depletes cytoplasmic AcCoA to preserve epigenetic stemness.

(**A**) Schematic of the molecular pathways involving compartmentalization of mitochondrial and cytoplasmic AcCoA. Model depicts how reduction in cytoplasmic AcCoA inhibits acquisition of effector functions through epigenetic changes. (**B** and **C**) Quantifications of total cellular AcCoA, cytoplasmic citrate, and nucleocytosolic AcCoA from cells treated in the indicated conditions. Data are means ± SEM and are representative of two independent experiments with at least three culture replicates. (**D**) Representative immunoblot showing reduced protein acetylation on Lys residues in the indicated conditions, with quantification at right. Data are means ± SEM and are representative of two independent experiments. (**E**)

Drosophila DNA spike-in normalized quantifications of H3K9Ac and H3K27Ac enrichment by ChIP-PCR at the *Ifng* locus. Data are means ± SEM and are representative of two independent experiments with at least three culture replicates. (**F**) Representative genomic alignments of H3K9Ac ChIP-seq and RNA-seq measurements showing reduced deposition of acetylation or transcripts at the *Ifng* locus of $CD8^+$ Tcells treated in the indicated conditions. Black bars under the tracks represent the called common peaks in $\uparrow[K^+]_e$ and control. Black boxes are sites of acetylation at transcription start site (TSS) and enhancer loci. (**G**) Representative genomic alignments of H3K9Ac deposition on the inhibitory receptor gene loci *Pdcd1* (C*D*279), *CD244* (2B4), *Havcr2* (Tim-3), and *Klrg1.* (**H**) Left: Volcano plot depicting a subset of effector genes and inhibitory receptors with reduced H3K9Ac deposition in $\uparrow[K^+]_e$ relative to control T cells. Right: GSEA with statistical analysis of effector genes and gene set associated with loss of stemness ($Tim3^+$ versus $CXCR5^+$ UP). Abundance is represented as relative change (*x* axis, calculated from normalized read counts of the peaks annotated to nearest TSS) versus significance (*y* axis). (**I**) Volcano plots representing reduced H3K9Ac deposition of effector genes that showed differential chromatin accessibility in ATAC-seq datasets (GSE86797) of the indicated conditions. Abundance is represented as relative change (*x* axis) versus significance (*y* axis). ChIP-seq experiments for each condition were performed with two independent cultures. $*P < 0.05$, $**P < 0.01$, $***P < 0.001$ (two-tailed *t* tests).

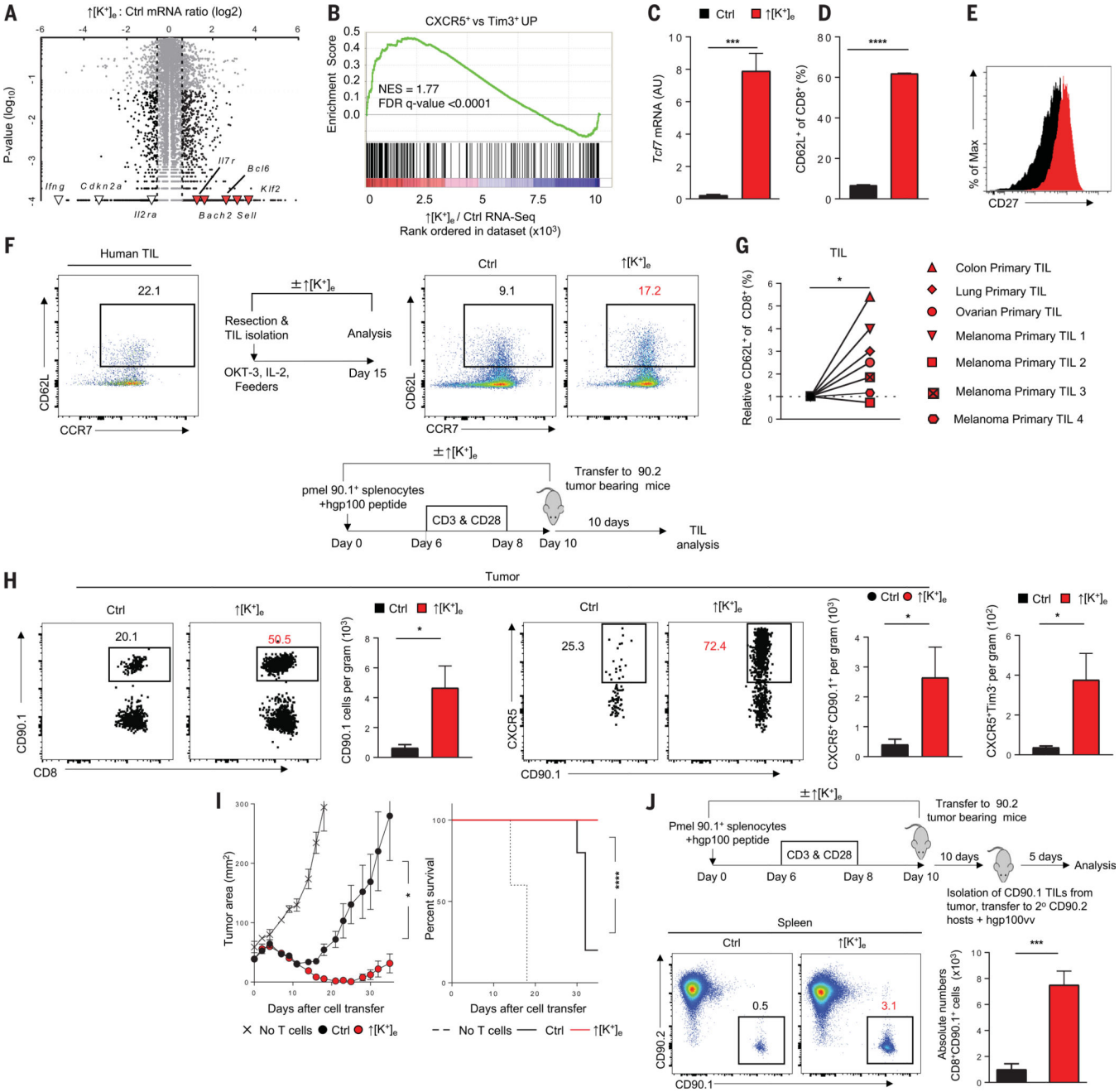

Fig. 4. Exposure to increased $[K^+]_e$ limits terminal effector differentiation in murine and human Tcells, enhancing persistence and antitumor function.

(**A**) Volcano plot representing differentially expressed genes analyzed by RNA-seq of $CD8^+$ T cells cultured in $\uparrow[K^+]_e$ versus control. Genes highlighted on the positive axis show enrichment of memory gene signature in $\uparrow[K^+]_e$; effector genes with decreased expression are shown on the negative axis. Abundance is represented as relative change (*x* axis) versus significance (*y* axis). (**B**) GSEA of $\uparrow[K^+]_e$ versus control comparing with genes enriched in $CXCR5^+$ versus $Tim3^+$high dataset. (**C**) Quantification (left) of *Tcf7* mRNA transcripts relative to actin as determined by reverse transcription PCR. (**D**) Quantification of $CD62L^+$.

(**E**) $CD27^+$ cells in pmel $CD8^+$ T cells cultured in the indicated conditions. Data are means ± SEM and are representative of two (C) or three [(D) and (E)] independent experiments. (**F**) Representative FACS plots showing the starting population phenotype of $CD8^+$ TILs obtained from a fresh tumor digest of a melanoma patient, with schematic of in vitro culture conditions. (**G**) Quantifications of relative $CD8^+$ $CD62L^+$ yields of neoantigen-specific and $CD8^+$ TILs from various tumor types by culturing in $\uparrow[K^+]_e$ conditions. Data are means of culture replicates per patient sample. (**H**) Schematic of control or $\uparrow[K^+]_e$ T cell culture conditions and adoptive T cell transfer into mice bearing established B16 melanoma tumors. Representative FACS plots show percentages and absolute numbers of pmel (CD90.1), $CXCR5^+$, and $CXCR5^+$ $Tim3^-$ T cells present in tumors 10 days after adoptive transfer. Data are means ± SEM and are representative of two independent experiments with at least five mice per group. (**I**) Tumor growth curves (left) and survival rates (right) of mice bearing B16 tumors treated with pmel T cells cultured in control or $\uparrow[K^+]_e$. In vivo data shown are representative of three independent experiments with $n = 5$ to 10 mice per group. Tumor measurements were plotted as mean ± SEM for each data point; tumor treatment curves were compared by Wilcoxon rank sum test; animal survival was assessed by log-rank test. (**J**) Schematic of adoptively transferred CD90.1 TIL isolation from B16 tumors and secondary transfer to CD90.2 mice. Recall response of transferred TILs in CD90.2 host was assessed by challenging with recombinant vaccinia virus expressing gp100. Absolute numbers are from day 5 after viral challenge. Data are means ± SEM with $n \geq 5$ mice per group. $*P < 0.05$, $***P < 0.001$, $****P < 0.0001$ (two-tailed *t* tests).

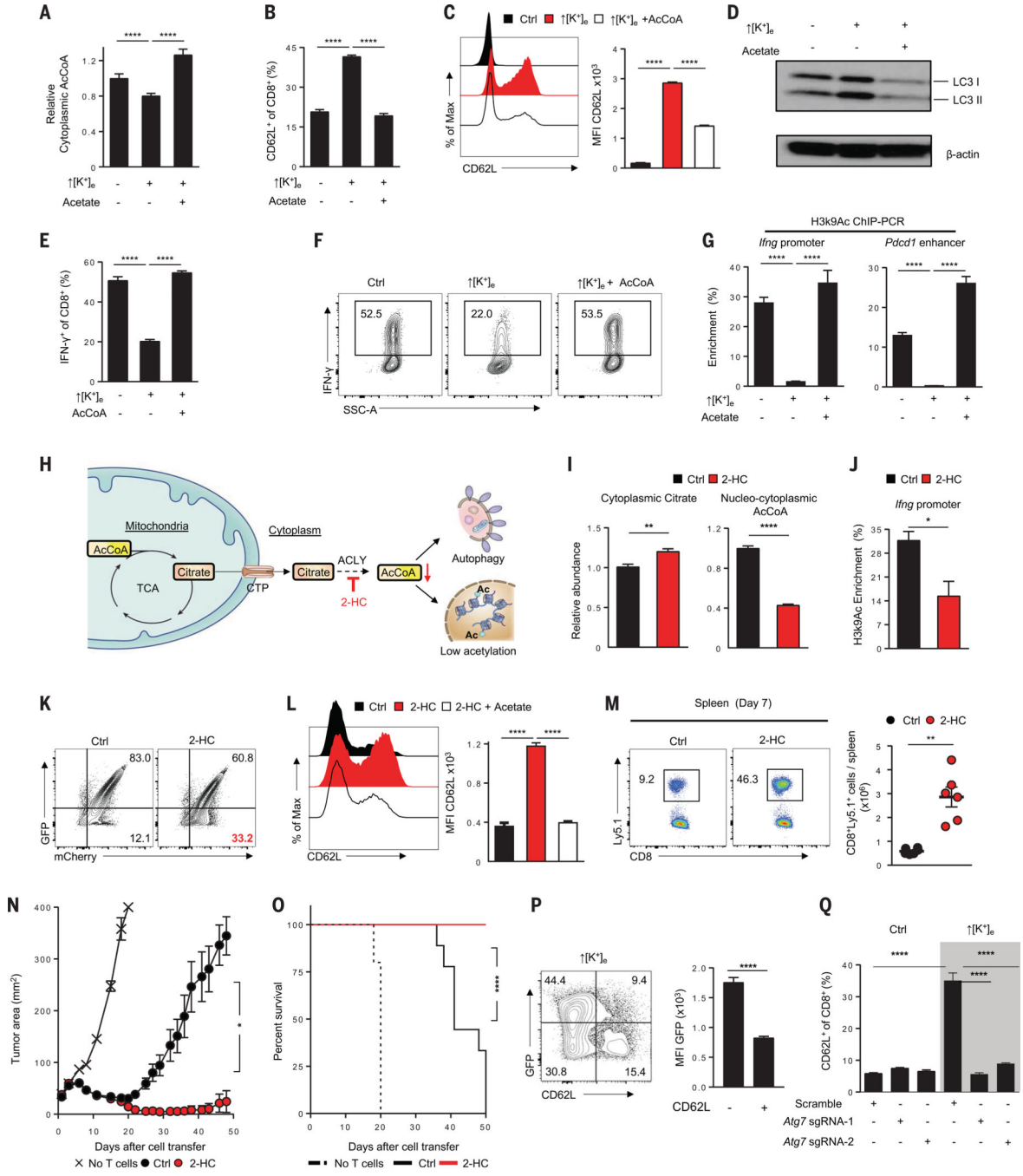

Fig. 5. Increased $[K^+]_e$-mediated metabolic reprogramming is mediated by AcCoA subcellular abundance and autophagy.

(**A**) Rescue of ↑$[K^+]_e$ effects on cytoplasmic AcCoA by external acetate (5 mM) supplementation. (**B** and **C**) Representative FACS plot quantifications of effects of external acetate (B) and electroporated AcCoA(50 μM) (C) on CD62L cell surface expression in $CD8^+$ T cells in the indicated conditions. Data are means ± SEM and are representative of two (A) or three [(B) and (C)] independent experiments. (**D**) Immunoblot showing reduction of autophagy in ↑$[K^+]_e$ by provision of external acetate. (**E** and **F**) Representative FACS

plots and quantification showing augmentation of IFN-γ cytokine expression by electroporation of external AcCoA (50 mM). Data are means ± SEM and are representative of two independent experiments. (**G**) Quantifications of H3K9Ac enrichment by ChIP-PCR at the *Ifng* and *Pdcd1* enhancer locus in the indicated conditions. Data are means ± SEM from at least three culture replicates. (**H**) Schematic of the molecular pathways, substrates, and associated enzymes involved in the generation of cytoplasmic AcCoA pools. CTP, citrate transporter; 2-HC, ACLY inhibitor (5 mM hydroxycitrate). (**I**) Quantification of cytoplasmic citrate and cytoplasmic AcCoA from the cells treated in the indicated conditions. (**J**) ChIP-PCR quantification showing reduced H3K9Ac deposition at the *Ifng* locus in 2-HC–treated cells. Data are means ± SEM and are representative of three (I) or two (J) independent experiments with $n = 3$ culture replicates per experiment. (**K**) Representative FACS plots of autophagy flux in the indicated conditions by measuring the loss of GFP in $mCherry^+$ populations. (**L**) Representative FACS plots showing effect of external acetate supplementation on CD62L expression in 2-HC–treated cells. Data are means ± SEM and are representative of two independent experiments with $n = 3$ culture replicates per experiment. (**M**) Representative flow cytometry analysis (left) and absolute number quantification (right) of transferred $Ly5.1^+$ $CD8^+$ T cells in the spleen of tumor-bearing mice on day 7 in the indicated conditions. Data are representative of two independent experiments with at least $n = 5$ mice per group. (**N** and **O**) Antitumor efficacy (left) and survival rates in mice (right) bearing B16 tumors treated with pmel T cells cultured in control ($n = 10$) or 2-HC ($n = 10$). Tumor measurements were plotted as mean ± SEM for each data point; tumor treatment curves were compared by Wilcoxon rank sum test; animal survival was assessed by log-rank test. Data are representative of two independent experiments. (**P**) Representative flow cytometry analysis and quantifications showing reduced autophagic flux in $CD62L^-$ populations. Data are means ± SEM and are representative of two independent experiments with $n = 3$ culture replicates per experiment. (**Q**) Representative flow cytometry quantification showing abrogation of increased CD62L expression driven by $\uparrow[K^+]_e$ upon genetic perturbation of *Atg7* (highlighted in gray). $^*P < 0.05$, $^{**}P < 0.01$, $^{****}P < 0.0001$ (two-tailed *t* tests).

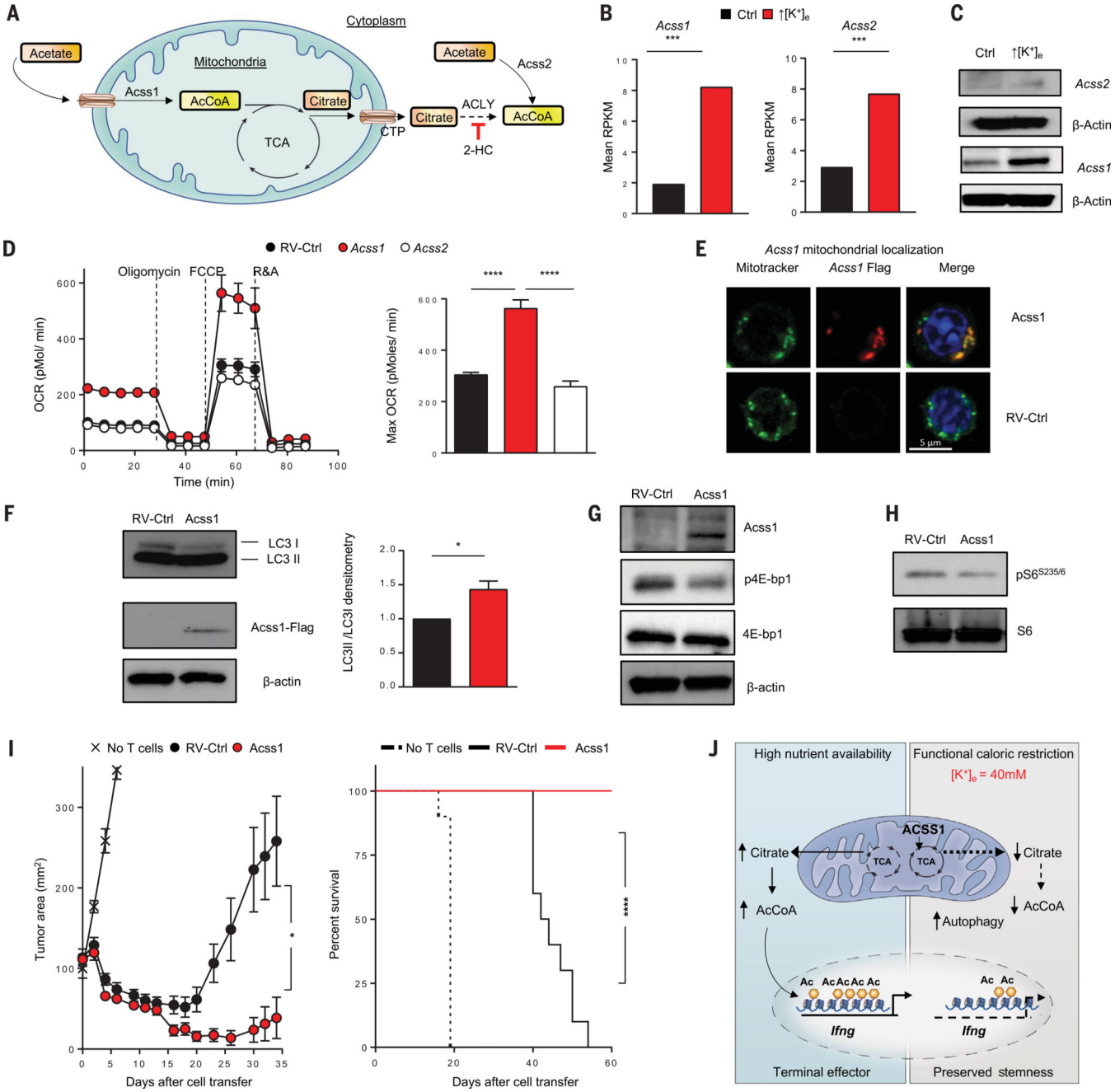

Fig. 6. Acss1 promotes mitochondrial metabolism to augment T cell persistence and antitumor activity.

(**A**) Schematic of the molecular pathways, substrates, and associated enzymes involved in the generation of mitochondrial and cytoplasmic AcCoA pools. (**B**) Quantifications showing the normalized mRNA transcripts of AcCoA synthetase (*Acss1* and *Acss2*). RPKM, reads per kilobase per million mapped reads. (**C**) Immunoblot showing protein expression of Acss1 and Acss2 in control or ↑$[K^+]_e$ T cells. (**D**) OCRs of control or Acss1- or Acss2-transduced $CD8^+$ pmel T cells were measured in real time under basal conditions in response to the indicated mitochondrial inhibitors. Data are means ± SEM and are

representative of two independent experiments. (**E**) Representative confocal images defining the localization of Acss1 in mitochondria. (**F**) Immunoblot densitometry of LC3b-I and LC3b-II in RV-control or Acss1 overexpression conditions. Data are means ± SEM of three independent immunoblots. (**G** and **H**) Immunoblot showing reduced phosphorylation of the nutrient-sensing kinase mTOR substrates p-4EBP and phosphor-S6 ($S^{235/236}$) in Acss1-overexpressing $CD8^+$ T cells. (**I**) Tumor growth (left) and animal survival curves (right) of sublethally irradiated mice bearing B16 tumors treated with T cells transduced with retrovirus control ($n = 10$) or Acss1-transduced T cells ($n = 10$). Tumor measurements were plotted as mean ± SEM for each data point; tumor treatment curves were compared by Wilcoxon rank sum test; animal survival was assessed by log-rank test. In vivo data shown are representative of two independent experiments. (**J**) Illustration showing dual role of potassium in limiting the acquisition of effector functions and preserving the stemness of T cells. $*P < 0.05$, $***P < 0.001$, $****P < 0.0001$ (two-tailed *t* tests).